Operation and calibration of the Silicon Drift Detectors of the ALICE experiment during the 2008 cosmic ray data taking period

B. Alessandro,[a] **S. Antinori,**[b] **R. Bala,**[c,a] **G. Batigne,**[d] **S. Beolè,**[c,a] **E. Biolcati,**[c,a]
N. Bock Garcia,[e] **E. Bruna,**[c,1] **P. Cerello,**[a] **S. Coli,**[a] **Y. Corrales Morales,**[a,2] **F. Costa,**[f]
E. Crescio,[c] **P. De Remigis,**[a] **S. Di Liberto,**[g] **D. Falchieri,**[b] **G. Feofilov,**[h] **W. Ferrarese,**[c]
E. Gandolfi,[i,b] **C. Garcia,**[a,2] **L. Gaudichet,**[a] **G. Giraudo,**[a] **P. Giubellino,**[a]
T.J. Humanic,[e] **S. Igolkin,**[f] **M. Idzik,**[c,a,3] **S.K. Kiprich,**[j] **A. Kisiel,**[f] **A. Kolozhvari,**[h]
I. Kotov,[e] **J. Kral,**[k] **S. Kushpil,**[l] **V. Kushpil,**[l] **R. Lea,**[c,a] **M.A. Lisa,**[e] **M.I. Martinez,**[a,4]
A. Marzari Chiesa,[c,a] **M. Masera,**[c,a] **M. Masetti,**[i,b] **G. Mazza,**[a] **M.A. Mazzoni,**[g]
F. Meddi,[m,g] **L.M. Montano Zetina,**[c,a,5] **M. Monteno,**[a] **B.S. Nilsen,**[e,6] **D. Nouais,**[a]
F. Padilla Cabal,[a,2] **V. Petráček,**[k] **M.G. Poghosyan,**[c,a] **F. Prino,**[a] **L. Ramello,**[n]
A. Rashevsky,[o] **L. Riccati,**[a] **A. Rivetti,**[a] **S. Senyukov,**[n] **M. Siciliano,**[c,a] **M. Sitta,**[n,7]
M.A. Subieta Vasquez,[c,a] **M. Sumbera,**[l] **L. Toscano,**[a] **F. Tosello,**[a] **D. Truesdale,**[e]
G.M. Urciuoli,[g] **A. Vacchi,**[o] **S. Vallero,**[p] **A. Werbrouck,**[q,a] **G. Zampa**[o] **and G. Zinovjev**[r]

[a]*Istituto Nazionale di Fisica Nucleare, Sezione di Torino,*
Turin, Italy

[b]*Istituto Nazionale di Fisica Nucleare, Sezione di Bologna,*
Bologna, Italy

[c]*Dipartimento di Fisica Sperimentale, Università di Torino,*
Turin, Italy

[d]*SUBATECH, Ecole des Mines de Nantes, Université de Nantes,*
CNRS/IN2P3, Nantes, France

[e]*Department of Physics, Ohio State University, Columbus, OH, U.S.A.*

[f]*European Organization for Nuclear Research, CERN, Geneva, Switzerland*

[1]Presently at Physics Department, Yale University, New Haven, U.S.A.
[2]Also Instituto Superior de Tecnologìas y Ciencias Aplicadas, La Habana, Cuba
[3]Presently at Faculty of Physics and Applied Computer Science, AGH University of Science and Technology, Krakow, Poland
[4]Also Benemerita Universidad Autonoma de Puebla, Puebla, Mexico
[5]On leave from Physics Department, Centro de Investigacion y de Estudios Avanzados del IPN, Mexico
[6]Presently at Department of Physics, Creighton University, Omaha, NE, U.S.A.
[7]Corresponding author.

2010 JINST 5 P04004

^{g}*Istituto Nazionale di Fisica Nucleare, Sezione di Roma,*
  Rome, Italy

^{h}*V. Fock Institute for Physics, St. Petersburg State University,*
  St. Petersburg, Russia

^{i}*Dipartimento di Fisica, Università di Bologna, Bologna, Italy*

^{j}*National Science Center, Kharkiv Institute of Physics and Technology,*
  Kharkiv, Ukraine

^{k}*Faculty of Nuclear Sciences and Physical Engineering, Czech,*
  Technical University in Prague, Czech Republic

^{l}*Nuclear Physics Institute, Academy of Sciences of the Czech*
  Republic, Czech Republic

^{m}*Dipartimento di Fisica, Università di Roma "La Sapienza",*
  Rome, Italy

^{n}*Facoltà di Scienze, Università del Piemonte Orientale and INFN,*
  Alessandria, Italy

^{o}*Istituto Nazionale di Fisica Nucleare, Sezione di Trieste,*
  Trieste, Italy

^{p}*Physikalisches Institut, University of Heidelberg,*
  Heidelberg, Germany

^{q}*Facoltà di Scienze, Università di Torino, Turin, Italy*

^{r}*Bogolyubov Institute for Theoretical Physics, Kiev, Ukraine*

E-mail: sitta@to.infn.it

ABSTRACT: The calibration and performance of the Silicon Drift Detector of the ALICE experiment during the 2008 cosmic ray run will be presented. In particular the procedures to monitor the running parameters (baselines, noise, drift speed) are detailed. Other relevant parameters (SOP delay, time-zero, charge calibration) were also determined.

Contents

1 Introduction

High-energy heavy-ion physics aims to study and attempts to understand how collective phenomena and macroscopic properties, involving many degrees of freedom, emerge from the microscopic laws of elementary-particle physics. The most interesting case of collective phenomena is the occurrence of phase transitions in quantum fields at characteristic energy densities; this would affect the current understanding of both the structure of the Standard Model at low energy and of the evolution of the early Universe. In ultra-relativistic heavy-ion collisions, energy densities are expected to reach and exceed the critical energy density $\varepsilon_c \simeq 1\,\mathrm{GeV\,fm^{-3}}$, predicted by lattice calculations of Quantum ChromoDynamics (QCD) for a phase transition of nuclear matter to a deconfined state of quarks and gluons, thus making the QCD phase transition the only one predicted by the Standard Model that is presently within reach of laboratory experiments.

ALICE [1, 2] is a general-purpose heavy-ion experiment primarily designed to study the physics of strongly interacting matter and the quark-gluon plasma formed in nucleus-nucleus collisions at the LHC [3]. Its detectors measure and identify mid-rapidity ($-0.9 \leq \eta \leq 0.9$) hadrons, electrons and photons produced in the collision and reconstruct particle tracks, including short-lived ones, in an environment with large multiplicity of charged particles. A forward muon arm detects and identifies muons covering a large rapidity domain ($-4.0 \leq \eta \leq -2.4$). Hadrons, electrons and photons are detected and identified in the central rapidity region by a complex system

of detectors immersed in a moderate (0.5 T) magnetic field. Tracking relies on a set of high resolution detectors: an Inner Tracking System (ITS) consisting of six layers of silicon detectors, a large-volume Time-Projection Chamber (TPC) and a high-granularity Transition-Radiation Detector (TRD). Particle identification in this central region is performed by measuring energy loss in the ITS and TPC, transition radiation in the TRD, Time Of Flight (TOF) with a high-resolution array of multigap Resistive Plate Chambers, Cherenkov radiation with a High-Momentum Particle Identification Detector (HMPID), photons with a high granularity crystal PHOton Spectrometer (PHOS) and a low granularity electromagnetic calorimeter (EMCAL). Additional detectors located at large rapidities complete the central detection system to characterize the event and to provide the interaction triggers.

The Inner Tracking System [2, 4] is the tracking detector nearest to the interaction point, and covers the $|\eta| < 0.9$ rapidity range. Its basic functions are the determination of primary and secondary vertices, the improvement of the momentum and angular resolution of tracks reconstructed in the external Time Projection Chamber, as well as the tracking and identification of particles missed by the TPC.

The ITS consists of six coaxial cylinders: two innermost ones form the Silicon Pixel Detectors (SPD), two intermediate ones the Silicon Drift Detectors (SDD), two outermost ones the Silicon Strip Detectors (SSD). The number, position and segmentation of the layers have been optimized for efficient track finding and high impact parameter resolution. Due to the enhanced particle density and in order to achieve the required resolution (of the order of $12 \div 30$ μm on the $r\varphi$ direction [2]), different techniques are exploited to reconstruct in two dimensions the intersection point of a particle with each layer: in this way the whole ITS allows to precisely reconstruct the trajectory of particles directly emerging from the interaction point. Moreover the SDD and SSD also provide dE/dx information needed for ITS particle identification, while the fast-OR of the SPD read-out chips is used as a Level-0 trigger signal.

The physics programme of ALICE includes data taking during the pp runs and dedicated proton-nucleus runs to provide reference data and to address a specific pp physics programme. Heavy ion running will primarily be done with Pb ions, but data with lighter ions will also be collected in order to study the energy-density dependence of the measured phenomena. A prolonged period of cosmic ray data taking (henceforth called "cosmic runs") is foreseen for the commissioning phase of various subdetectors; an extended programme of cosmic runs for physical analyses has also been planned.

In section 2 the hardware, the front-end electronics and the data acquisition of the Silicon Drift Detectors are described. In section 3 the acquisition runs used to calibrate and monitor the detectors are presented. The analysis of data taken during the 2008 cosmic run period and their use for detector alignment and charge calibration are discussed in detail in section 4. Final conclusions and future perspectives are addressed in section 5.

2   The Silicon Drift Detectors

The Silicon Drift Detectors (SDD) equip the two intermediate layers (numbered 3 and 4) of the ITS, where the charged particle density is expected to reach up to 7 cm^{-2} [2].

Table 1. SDD main characteristics.

Sensitive area		70.17×75.26 mm^2	
HV (nominal)	-1800 V	Bias (MV)	-40 V
Anode pitch	294 μm	Drift velocity	$\sim$6.5 μm/ns
Av. z resolution	25 μm	Av. $r\varphi$ resolution	35 μm

One SDD module consists of a drift detector and its front-end electronics. It was produced from very homogeneous high-resistivity (3 kΩ cm) 300 μm thick Neutron Transmutation Doped (NTD) silicon [5, 6]. It has a sensitive area of 70.17($r\varphi$) $\times$ 75.26(z) mm^2 and a total area of 72.50 $\times$ 87.59 mm^2. The sensitive area of a detector is split into two drift regions, with electrons moving in opposite ($r\varphi$) directions, by a central cathode kept at a nominal voltage of -1800 V. In each drift region, and on both detector surfaces, 291 p$^+$ cathode strips, with 120 μm pitch, fully deplete the detector volume and generate a drift field of $\sim$ 500 V/cm parallel to the wafer surface. A second medium voltage (MV) supply of -40 V keeps the biasing of the collecting region independent of the drift voltage, and directs the electron charge toward the collecting anodes.

Each drift region is equipped with 256 anodes with 294 μm pitch (along the z direction) to collect the charges, and three rows of 33 MOS charge injectors (20 $\times$ 100 μm^2 each) used in monitoring the drift velocity as a function of the anode number for each SDD module [7]. This velocity depends on temperature as $v_{\text{drift}} \propto T^{-2.4}$ [8], giving a 0.8%/K variation at room temperature. It is about 6.5 μm/ns at the bias voltage of -1.8 kV and at the normal operating temperature (around 20–25°C).

The space precision along the drift direction ($r\varphi$), as obtained during beam tests of full-size prototypes, depends on the drift distance and is better than 38 μm over the whole detector surface. The precision along the anode axis (z), also dependent on drift distance, is better than 30 μm over 94% of the detector surface and reaches 60 μm close to the anodes, where a fraction of clusters affects only one anode. The average values are 35 μm ($r\varphi$) and 25 μm (z) respectively [9].

The main characteristics of each detector are summarized in table 1; a sketch of one sensor is depicted in figure 1

The SDD modules are mounted on linear support structures called *ladders*: on layer 3 (at $r = 14.9$ cm) there are 14 ladders with 6 modules each, while on layer 4 (at $r = 23.8$ cm) there are 22 ladders with 8 modules each, for a total of 260 modules. To ensure full angular coverage ladders and modules are assembled with an overlap of the sensitive areas larger than 580 μm in both $r\varphi$ and z directions (corresponding to about 2% of the module area). During the 2008 cosmic run $\sim$ 98% of the SDD modules were included in the acquisition.

During the module assembling on ladders, the position of each module was precisely measured with respect to a fixed point (a ruby sphere fixed to the ladder structure). The resulting residual between the real and nominal position is centered on 0 and has an RMS of about 20 μm for both z and $r\varphi$ directions.

All 260 modules were characterized before being assembled in ladders using an infrared laser (λ = 980nm) [11]. Charges were injected in $> 100,000$ positions per module, and residuals be-
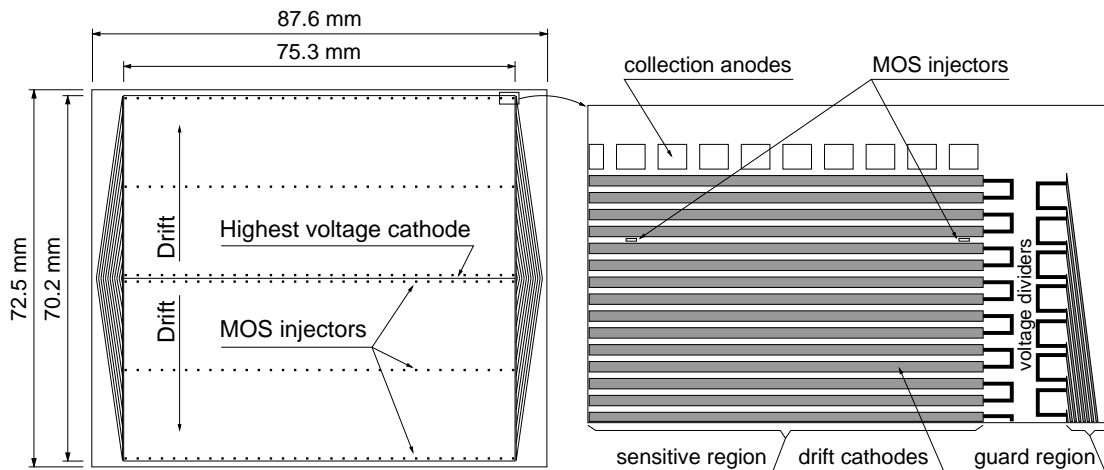
Figure 1. Layout of the ALICE SDD modules. The left panel shows a whole module, the right panel is an enlargement of the collecting anode region.

tween the indirectly reconstructed coordinates (from measured ADC counts) and the known laser ones were computed. In this way a map of systematic deviations of drift coordinate (mainly caused by non-constant drift field influenced by voltage supplied by non-linear voltage dividers and in two cases by parasitic electric fields due to significant dopant inhomogeneities) was constructed for each detector, to be used to correct the time coordinate during the reconstruction stage.

The effects of irradiation on the sensitive region and in particular on the MOS injectors were evaluated by exposing a test setup to a 1 GeV electron beam [12] and to a π^- beam of 100 GeV momentum [13]. The total exposure was equivalent to 10 years of ALICE operation as far as the bulk damage is concerned. The detector was found to be sufficiently radiation resistant for the anode current, the voltage distribution and the operation of the MOS injectors.

2.1 Front-end electronics and readout

The SDD front-end electronics is based on three types of ASICs, two of them, PASCAL and AMBRA, assembled on an hybrid circuit (shown in figure 2 on its assembly jig) which is directly bonded to the sensor, and one, CARLOS, located at each end of a ladder.

Each PASCAL chip, which reads signals from 64 anodes, contains three functional blocks: preamplifier, analogue storage and Analogue-to-Digital Converter (ADC). Each AMBRA chip receives the input from a PASCAL, and is a digital four-event buffer which performs data derandomisation, baseline equalization on an anode-by-anode basis and 10-bit to 8-bit non-linear data compression. The output of an AMBRA is fed to a CARLOS chip, which performs data compression and bidimensional two-threshold zero suppression. The nominal power supplies are 2.5 V for each PASCAL, AMBRA and CARLOS respectively. The average power dissipation of each PASCAL-AMBRA front-end channel is about 6 mW. A cooling system is used to take away the power dissipated by the front-end electronics and to maintain a temperature stability of the order of 0.1 K [10]. The system uses demineralized water as cooling agent and is divided into 52 independent circuits. In order to provide leak-tightness inside the detector the water pressure is kept below the atmospheric one, while the dew point in the cavern fixes the minimum water temperature to
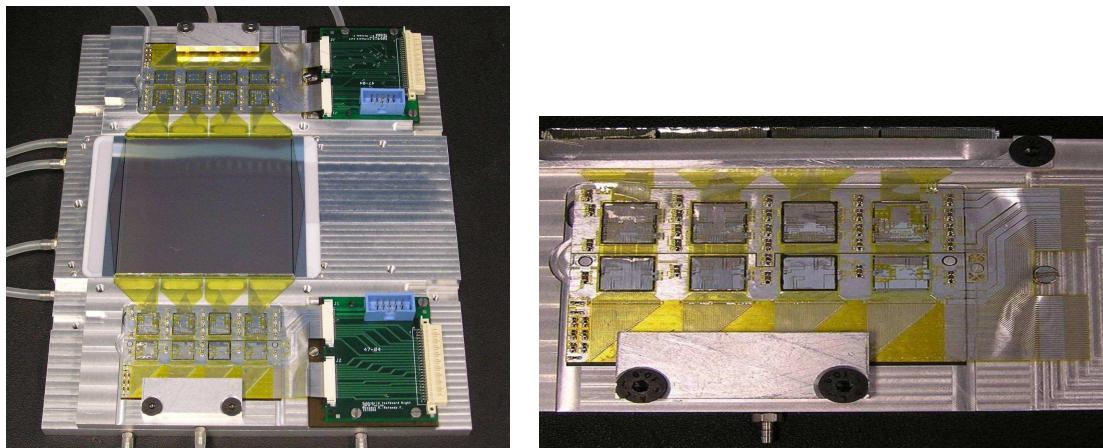
Figure 2. Left: A Silicon Drift Detector on the assembly jig with the two front-end hybrids connected, via their test extensions, to test interface circuits. Right: A single hybrid on its assembly jig: the four chips on the top row are the PASCALs, the ones on the bottom row are the AMBRAs.

19 °C. These conditions are constantly monitored by a dedicated interlock system. Moreover the water flow is measured in every circuit in order to assure adequate power absorption.

The signal generated by an SDD anode feeds the PASCAL amplifier-shaper which has a peaking time of 40 ns and a dynamic range of 32 fC (corresponding to the charge released by an 8-MIP particle hitting near the anode). The amplifier output is sampled at 40 MHz by a ring analogue memory with 256 cells per anode. On a run-by-run basis, PASCAL chips can be programmed to use half of the 40 MHz nominal frequency for the sampling, thus reducing the amount of data and, therefore, the sub-system readout dead-time. When a Level0 (L0) trigger is received, the SDD BUSY is immediately set and after a programmable delay which accounts for the L0 latency (1.2 μs) and the maximum detector drift time ($\sim$5 μs) the analogue memories are frozen. The BUSY being still set, their contents are then digitised by a set of 10-bit linear successive-approximation ADCs which write the data into one of the free AMBRA buffers. The digitisation can be aborted by the absence of the Level1 trigger or by the arrival of a Level2-reject signal: in both cases, the front-end electronics resets the SDD BUSY and returns to the idle state. On the successful completion of the analogue-to-digital conversion the SDD BUSY is reset if at least one buffer is still available in the AMBRAs.

As soon as the conversion is completed, all the AMBRAs transmit the data in sequence to the CARLOS chips. The zero suppression is performed by a 2-dimensional 2-thresholds algorithm: to be accepted as a valid signal, the ADC counts in a memory cell must exceed the higher threshold and have at least one neighbour above the lower one or viceversa. This allows to suppress noise spikes and to preserve as much as possible the samples in the tail of the signals [14]. With no additional dead time, using this algorithm the CARLOS chips reduce the SDD event size by more than one order of magnitude. They also format the data and feed the Gigabit Optical Link (GOL) ASICs which in turn send the data to the DAQ electronics via an optical fiber (about 100 m long).

The three ASICs embed a JTAG standard interface, which is used to download control information into the chips before the data taking. By means of the same interface it was possible to test each chip after the various assembly stages. A programmable test pulse generator on PASCAL allows a fast, yet detailed, test of the whole chain for calibration purposes.

2.2 Data acquisition

In the counting room, 24 VME boards, CARLOSrx [15], concentrate the data coming from the 260 SDDs into 24 Detector Data Link (DDL) channels and embody the trigger information in the data flow. Each CARLOSrx board controls up to 12 CARLOS chips. CARLOSrx also uploads in parallel the configuration parameters received over the DDL to the ladder front-end electronics it controls and monitors the error-flag words embedded in the data flow coming from the CARLOS chips in order to signal potential Single-Event Upsets (SEU) on the ladder electronics.

The CARLOSrx boards are arranged in three VME crates, one devoted to the acquisition of all modules on layer 3 and the other two for the modules of layer 4. Each VME crate is equipped with a VME CPU card used to load the board's firmware; this operation can be performed remotely by the operator from the experiment's control room.

Each CARLOSrx board is connected via an optical link to one input of a D-RORC (DAQ ReadOut Receiver Card) [16] PCI card (the D-RORC has two outputs and sends an exact copy of the data both to the DAQ and to the High-Level Trigger system). Since a DAQ PC can host a maximum of six D-RORC cards, during the 2008 cosmic data taking period presented here four Local Data Concentrator (LDC) computers were used to manage the SDD acquisition. Each LDC interfaces with the main run control programs, performs data collection and sub-event building, stores data locally and transfers them to the Global Data Collector (GDC) nodes if requested. During 2008 one GDC was dedicated to SDD standalone data taking. The GDC collects sub-events from the LDCs, performs the event building and stores data either locally or on a mass-storage system. Data recording can be disabled by software both on the LDC and GDC level. LDC's allow also to test the uploading of JTAG commands on the SDD front-end chips and to dump the data flow to a terminal for test and monitoring purposes.

When running in standalone mode the whole data taking process can be controlled by the SDD operator. In standalone mode the detector can acquire data using a pulsed trigger or a random trigger (whose rate can be set from 1 Hz up to 40 MHz). This allows to perform the calibration runs described below, to check the acquisition operation and to verify the detector performance (maximum event rate, detector occupancy due to noise, etc.). On the other hand when being part of a global acquisition run, the control is locked by the main Experiment Control System (ECS) and the SDD operator can only monitor the data flow and quality.

The SDD online monitoring is based on the Quality Assurance (QA) tools that are part of the ALICE offline framework, so as to provide online and offline functionality without code duplication. It is interfaced to the ALICE DAQ Data Quality Monitoring (DQM) framework AMORE (Automatic MOnitoRing Environment) [17], and is based on a publisher-subscriber approach. The SDD QA code is driven by an AMORE Agent that publishes in the AMORE Database the histograms generated by the SDD QA code itself. These histograms include the pattern of fired ladders and modules for each layer, and the charge map distributions of each half module (for a sampled event and integrated on all the analysed events). All the distributions can be retrieved from the database and visualized with the help of a custom Graphical User Interface (SDD GUI) that works as subscribing client. Distributions are plotted in groups selected by specific tabs. The currently available tabs provide the summary plots of the module pattern of each ladder for each layer, the DDL connections, the projection of the 2-D charge maps and the module maps.

3 Detector calibration

The three types of calibration runs described below have been implemented to monitor the performance of the detectors and to extract the relevant parameters for event reconstruction. These runs are initiated by the SDD operator. Events are triggered by the Local Trigger Unit (LTU) whose trigger rate is manually set to a very low frequency (not more than 4 Hz). After a predefined number of events is collected, the run is automatically stopped. The collected data are registered on both the LDCs (for immediate analysis) and on the mass storage system (for possible offline re-analysis). A dedicated Detector Algorithm (DA) is executed on the LDCs immediately after the end of a calibration run to analyze these data and calculate the calibration parameters that are needed in the reconstruction phase, namely anode-by-anode baseline, noise, gain and drift speed. Bad anodes and modules are also identified in this procedure. These calibration quantities provided by the DAs are stored in the Offline Condition DataBase (OCDB) for the SDD by means of the SHUTTLE framework [18]. The reconstruction code can then retrieve this information during the offline reconstruction by automatically selecting the most recent set of calibration data according to the run being analyzed.

During 2008 these runs were carried out once a day, when the detector was temporarily not part of a global run. For the future it is planned to run these calibrations during the LHC fill periods (every $\approx$ 24 hours).

3.1 Pedestal runs

Pedestal runs are special standalone runs performed every $\approx$ 24 hours with both zero suppression and baseline equalization disabled. Their analysis provides a measurement of the anode baseline (defined as the average signal value in ADC counts for each anode) and of the noise (defined as the standard deviation of the above determination of the average for each anode) both raw and corrected for common mode.[1] Moreover they can tag the noisy anodes which can be masked out during physics runs. The values of baselines and noise and the fraction of bad channels (around 0.5%) have all proven to be very stable during this entire data taking period.

When starting a pedestal run proper JTAG commands are sent to all modules to inhibit baseline equalization and set to zero the thresholds for zero suppression. The results of the pedestal DAs are the computation of the anode baselines and noise.

An example of baseline distribution as a function of the anode number for one half module is shown in figure 3 left; on the right panel of the same figure there is the distribution of baselines before equalization for all modules. Baselines are then equalized to bring them all to the same level of 20; the equalization value for each anode is inserted in the JTAG command sequence loaded on the AMBRA chips. The value of 20 was chosen as a compromise (to allow the 6-bit correction of high baseline anodes to be sufficient and to have a common baseline for all modules) between different requests: the maximum equalization correction is 6 bits (63 ADC units); the baseline should be as low as possible to take the best advantage of the 0-127 count range in which the ADC is not affected by the non-linear compression from 10 to 8 bits; on the other hand the baseline should not be so low that the noise can bring the ADC counts below zero.

---

[1]The algorithm for common mode correction is based on the measurement of coherent fluctuations (i.e. differences between the ADC counts and the baseline) of all the anodes in the same time bin.
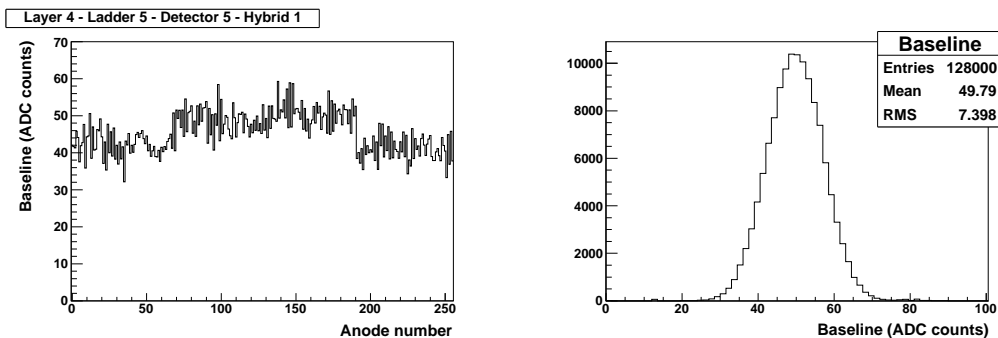
Figure 3. Left: Baseline distribution as a function of the anode number of an half module. Right: Distributions of all baseline values before equalization in a pedestal run.
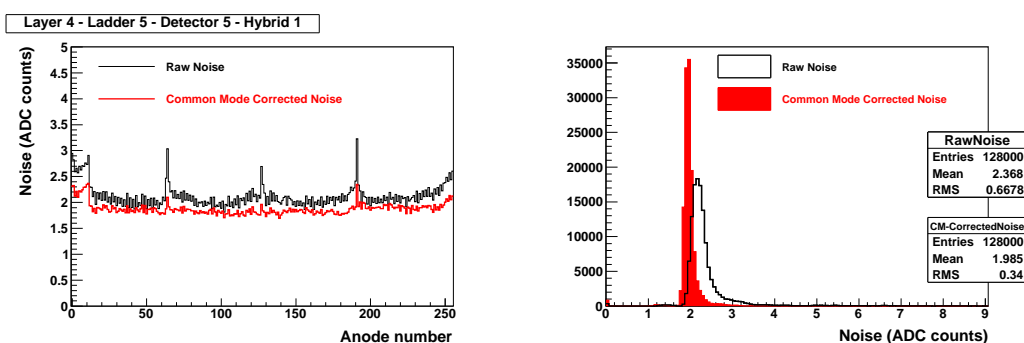

Figure 4. Left: Raw (black) and common mode corrected (red) noise distributions as a function of the anode number of an half module. Right: Distributions of raw (black) and common mode corrected (red) noise values for all anodes.

The same pedestal run is used to compute the noise, both raw and corrected for common mode, and to tag the noisy anodes. Anodes are marked as bad when the raw noise is < 0.5 or > 9 ADC counts; moreover anodes whose noise is greater than 4 times the mean noise of the entire module are also tagged as noisy. These bad anodes are masked out by inserting a proper bit mask in the JTAG commands sent to the AMBRA chips.

In figure 4 (left panel) the noise distribution as a function of the anode number of one half module is shown, while on the right panel of the same figure are the distributions of the raw and common mode corrected noise for all anodes. The peaks in the raw noise are located around anodes 0, 64, 128, 192 and 255, that is on the chip borders, since these anodes are more sensitive to the common mode noise. The removal of these peaks in the common mode corrected plot confirms the good performance of the implemented correction algorithm.

The measured noise is in agreement with the design value of 2 ADC counts, corresponding to an Equivalent Noise Charge (ENC) of 350 electrons. The signal peak (i.e. the cell with the maximum ADC counts in the cluster) is typically of 100 ADC counts over the baseline near the anodes (corresponding to a S/N ratio of about 50) and decreases with increasing drift distance. The signal peak dependence on drift time is detailed in section 4.3. The low and high thresholds for zero suppression are set for each hybrid to 2.2 and 4 times the average noise respectively.
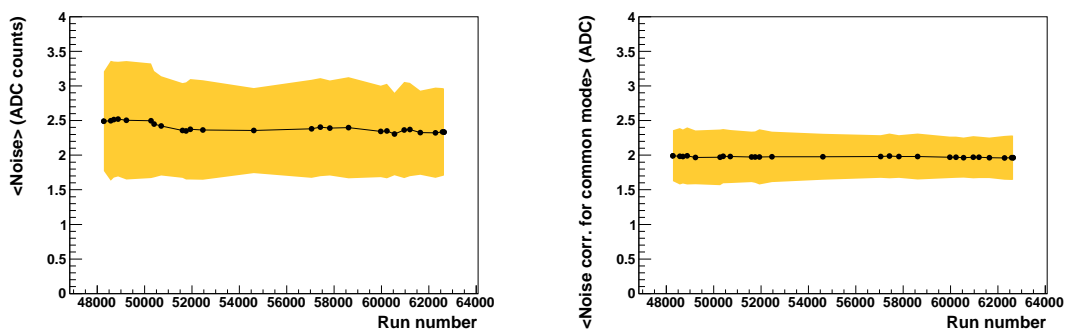
Figure 5. Raw (left) and common mode corrected (right) noise trend as a function of the run number during the 2008 cosmic run (from mid July to mid October); the yellow band is the RMS of the noise distributions.
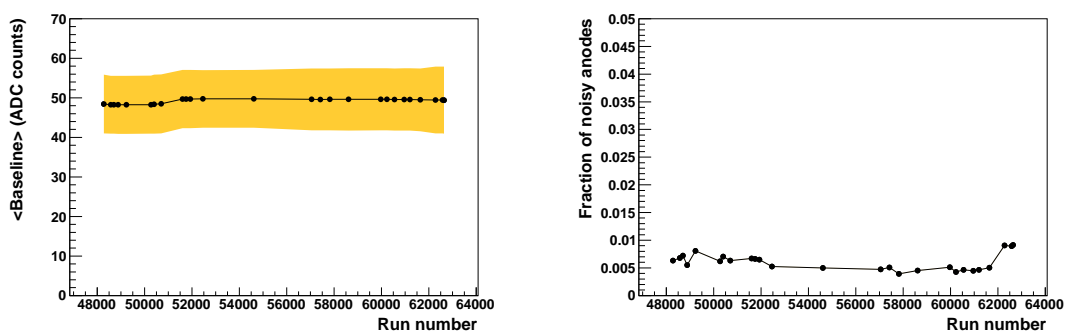

Figure 6. Trend of the baseline values (left) and of the fraction of bad anodes (right) as a function of the run number during the 2008 cosmic run (from mid July to mid October); the yellow band is the RMS of the baseline distribution.

The monitored parameters were very stable over a long period of time. In figure 5 the peak value of the noise distributions, both raw (left) and corrected for the common mode (right), is reported as a function of the run number from July 23rd to October 16th (the band is the RMS of each distributions). Similarly the mean value of the baseline distribution (figure 6 left) is also stable and the fraction of bad anodes (right) stays below 1% over the same period of time.

3.2 Pulser runs

Pulser runs are special standalone runs performed every ≈ 24 hours and collected without zero suppression, without baseline equalization and by sending the test pulse signal to the input of the PASCAL pre-amplifiers. One test pulse per event is used with a fixed amplitude of 100 DAC units, which is slightly lower than that of a MIP particle (which corresponds to 111 units). The analysis of a pulser run provides a measurement of the preamplifier gain (under the assumption of a linear behaviour of the preamplifier, which was verified during the test phase), and can tag the dead channels.

A pulser run is normally executed right after a pedestal run. Proper JTAG commands are sent to all modules to inhibit the zero suppression, set to zero the thresholds and the baseline equalization,
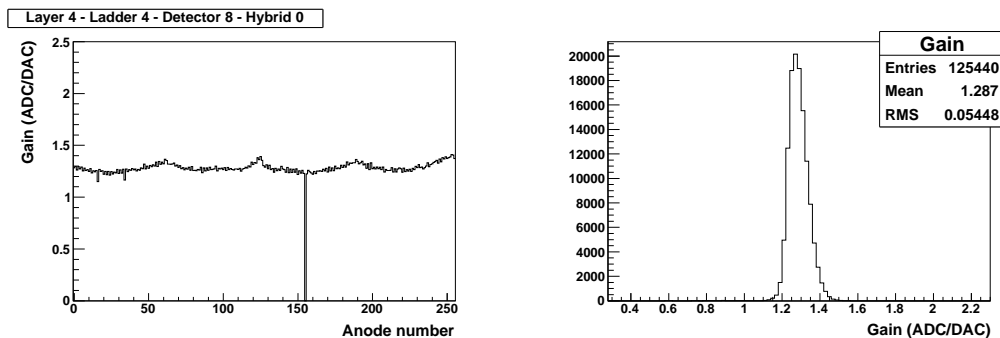
Figure 7. Left: Gain distribution as a function of the anode number of an half module; the bin with zero content corresponds to a dead channel. Right: Distributions of all gain values in a pulser run.

and activate the PASCAL test pulse generator, so that for each anode the test pulse is sent to the input of the front-end electronics. The result of pulser DAs is the determination of the gain for each channel. The information coming from the last pedestal run and the current pulser run are combined together and saved in the OCDB for the SDD.

An example of gain distribution as a function of the anode number of one half module is shown in figure 7 left; the bin with zero content corresponds to a dead channel. On the right panel of the same figure 7 there is the distribution of gains for all modules. This distribution is used to equalize the anode gain in the cluster finder algorithm, while the absolute dE/dx calibration is done with track based methods as described in section 4.3. This gain equalization correction is anyway very small since the gain distribution is very narrow.

The monitored parameters were very stable over a long period of time. In the left panel of figure 8 the mean value of the gain distribution is shown as a function of the run number from run July 23rd to October 16th (the band is the RMS of the distribution). The sudden reduction of gain value corresponds to the change from 40 MHz to 20 MHz sampling rate of the PASCAL amplifier; this reduction is connected to the different number of samplings taken on the impulse response of the front-end pre-amplifier, whose duration is about 100 ns. In the right panel of the same figure the fraction of dead channels stays below 2% during the same period of time. The fluctuations are also due to the fact that the sample of modules in acquisition was not constant during the data taking period.

3.3 Injector runs

A precise knowledge of the drift speed is a crucial element for the correct operation of any drift detector. Given its strict dependence on the detector temperature, the drift speed must be very frequently measured and monitored. To reach the design precision of 35 μm on a drift distance of as much as 35 mm (from the point farthest from the anodes) the drift speed must be known with an accuracy of better than 0.1%.

Injector runs are special standalone runs with zero suppression and with baseline equalization used to measure the drift speed. The MOS injectors are activated in order to inject charges in known positions (see figure 1).
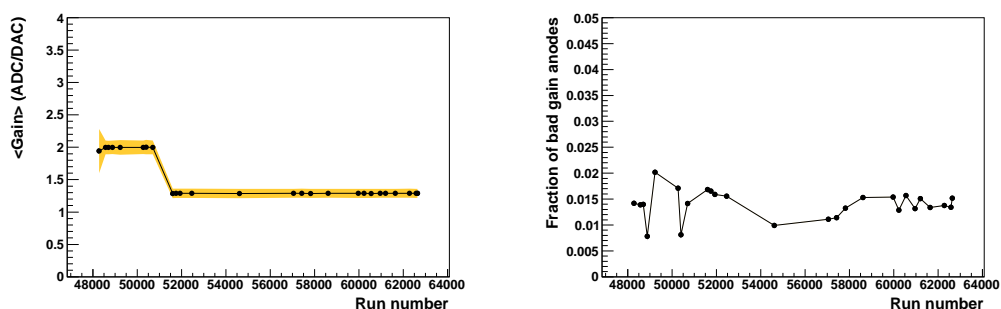
Figure 8. Trend of the gain values (left) and of the fraction of dead channels (right) as a function of the run number during the 2008 cosmic run (from mid July to mid October); the grey band is the RMS of the gain distribution. The sudden change of gain value corresponds to the change from 40 MHz to 20 MHz sampling rate.
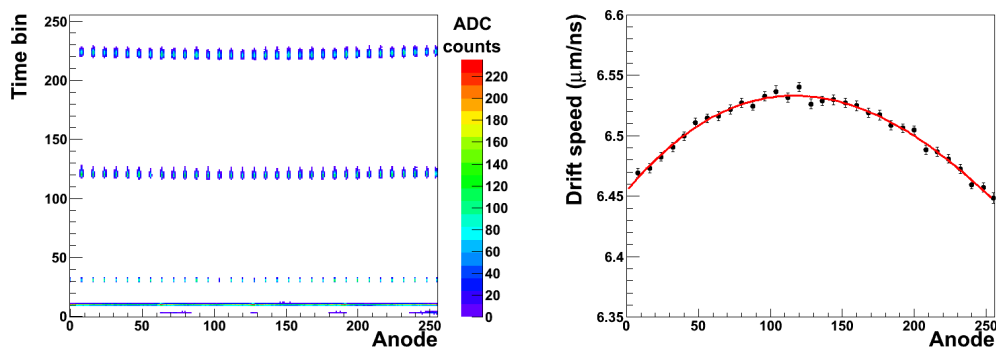

Figure 9. Left: Display of an injector event for a half module: the three MOS injector lines are clearly visible (the horizontal axis reports the anode number, the vertical axis the time bin; the color chart represents the quantity of charge collected by a single anode). Right: Drift values as a function of the anode number of one half module; each point represents the result of the fit on the three corresponding injectors.

In 2008 injector runs were performed every ≈ 6 hours. Proper JTAG commands are sent to all modules to enable the zero suppression, equalize the baselines and activate the MOS charge injectors. The result of the injectors DAs is the computation of the drift speed as a function of anode number for each SDD half-module. This information also is saved in the OCDB for the SDD subdetector to be used during reconstruction.

In the left panel of figure 9 the display of one injector event for one half module is shown: the image of the three injector lines are clearly visible, together with the pulse indicating the trigger time (continuous line at time bin 10). For each anode in front of which there are the MOS injectors (one anode out of eight) a linear fit of the three measured drift times is performed as a function of the known drift distance; the drift speed is then extracted from the slope of the fit. The operation is repeated on all the injector triplets of each module. An example of drift values as a function of the anode number of one half module is reported in the right panel of figure 9: the plot shows 33 drift values, one per MOS injector triplet, with a polynomial fit superimposed.

The drift speed depends on the local temperature as $T^{-2.4}$. The fact that heat sources (the
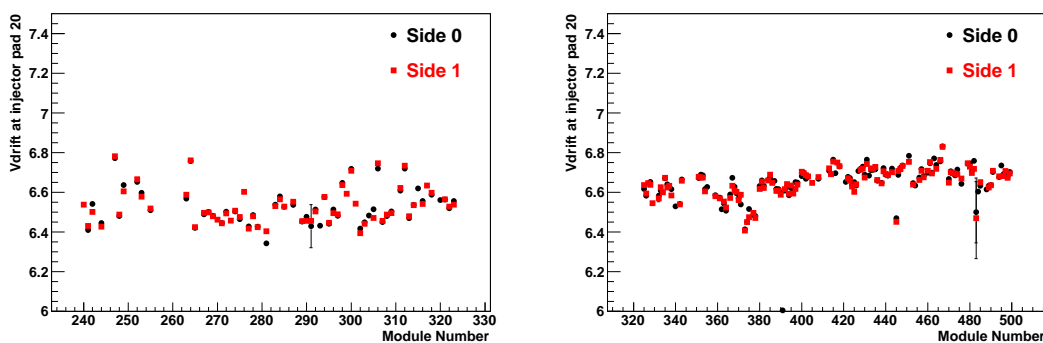
Figure 10. Mean drift speed, measured with the same injector pad for the two sides of a module, as a function of the module number for the Layer 3 (left) and Layer 4 (right) (where not shown, the error bars are smaller than the marker size; for two bad anodes the errors are large).

voltage dividers) are located at the sensor's edges explains the anode-by-anode dependence of the drift speed, lower near the warmer edges and higher in the colder mid region. For the same reason layer 3 has a drift speed systematically lower than layer 4 because being more internal it has a slightly higher temperature; this can be seen in figure 10, where the drift speed for all modules of each layer (measured with the same injector pad) is shown. Using a nominal value of 1350 $cm^2V^{-1}s^{-1}$ for the electron mobility at 293 K in n-type silicon with a 3 kΩ cm resistivity, and assuming that the mobility scales as $T^{-2.4}$, one can estimate an operating temperature of about 298 K for Layer 3 and 295 K for Layer 4. The observed module-by-module spread of drift speed values is mostly due to different operation temperatures (up to 2-3°C according to the simple model described above) rather then to differences in dopant concentration.

Also the mean drift speed was very stable over the entire period. In the left half of figure 11 the drift speed of one particular anode is plotted as a function of the day since the beginning of the cosmic run. In addition special 1 hour runs were collected in which the average drift speed was measured every minute; the fluctuations, expressed as the ratio of the distribution RMS to the mean, were $\simeq 0.07\%$ for most of the modules, as shown in the right half of figure 11. Due to the strong dependence of the drift speed on the temperature, these plots provide a tool to monitor (both online and offline) the stability of the sensor temperature during the data taking.

4 Operation and calibration during the 2008 cosmic run

4.1 SOP delay calibration

As explained in subsection 2.1 a proper delay must elapse between the trigger arrival time and the memories stop, so that the memory columns which contain the actual data can send them to ADC. A memory depth of 256 cells with a 40 MHz sampling rate defines a 6.4 μs time window, which must contain the signal of all charged particles crossing the detector, taking into account that the maximum drift time is $l_{det}/v_{drift} \simeq 3.5$ cm/6.5 μm/ns $\simeq 5.4$ μs. This Start Of Process (SOP) delay has to be tuned according to the trigger type, and during the 2008 data taking this was
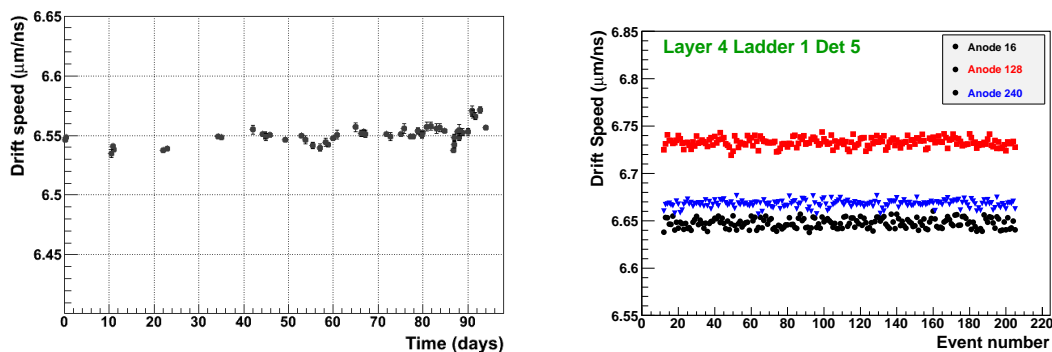
Figure 11. Left: Drift speed of one anode as a function of time (days since the beginning of the 2008 cosmic run). Right: drift speed of three anodes of a half module as a function of the event number in a special 1 hour run.

done during the T12 injection test. The aim is to center the SDD acquisition time window on the observed particle times.

The T12 injection test was one of the LHC commissioning tests. It consisted in injecting proton bunches into the T12 transfer line, which is the beam line connecting the SPS to the LHC sector 1–2. The beam was then dumped in the TED absorber about 300 m upstream of the ALICE detector. Each bunch consisted of $5 \cdot 10^9$ p at the SPS energy (450 GeV), and was injected every ~ 50 s. When the beam was dumped, a shower of secondary particles was produced and a certain fraction reached ALICE illuminating the central detectors. An example of one such event collected by the SDD is shown in figure 12.

The SOP delay scan was performed for both 40 and 20 MHz sampling rate. The technique consisted in collecting a certain amount of events with a given SOP delay value. A preliminary check on the detector occupancy was done, and it turned out that ~ 20 events per SOP delay value were enough. Then the drift time distribution of the saved data was determined offline using custom software tools without any event reconstruction. The overall procedure was repeated in steps of 10 SOP delay units (25 ns) from 110 to 140 (2750 to 3500 ns). The optimal value resulted in the range 120-125 SOP delay units (3000-3125 ns) for both 20 and 40 MHz sample rate.

As an example figure 13 shows the distribution of the particle drift times on Layer 4 sampled at 40 MHz for the four different SOP delay values examined. Clearly 140 delay units are too many, since the distribution is truncated at small drift times, while 110 are too few, since the same distribution is too close to the end of the time bin range. With 120 and 130 SOP delay units the drift time distributions are better centered within the 256 time bins, so 125 units were chosen.

4.2 Time-zero calibration

Another parameter measured during the 2008 commissioning is the time-zero, that is the time offset that has to be subtracted (half-module by half-module) from all measured drift times to obtain the actual particle time. Two strategies have been developed based on simulated data.

The first method consists in determining the minimum drift time from the time distribution of all measured clusters. The rising part of this distribution at small drift times, which in the ideal
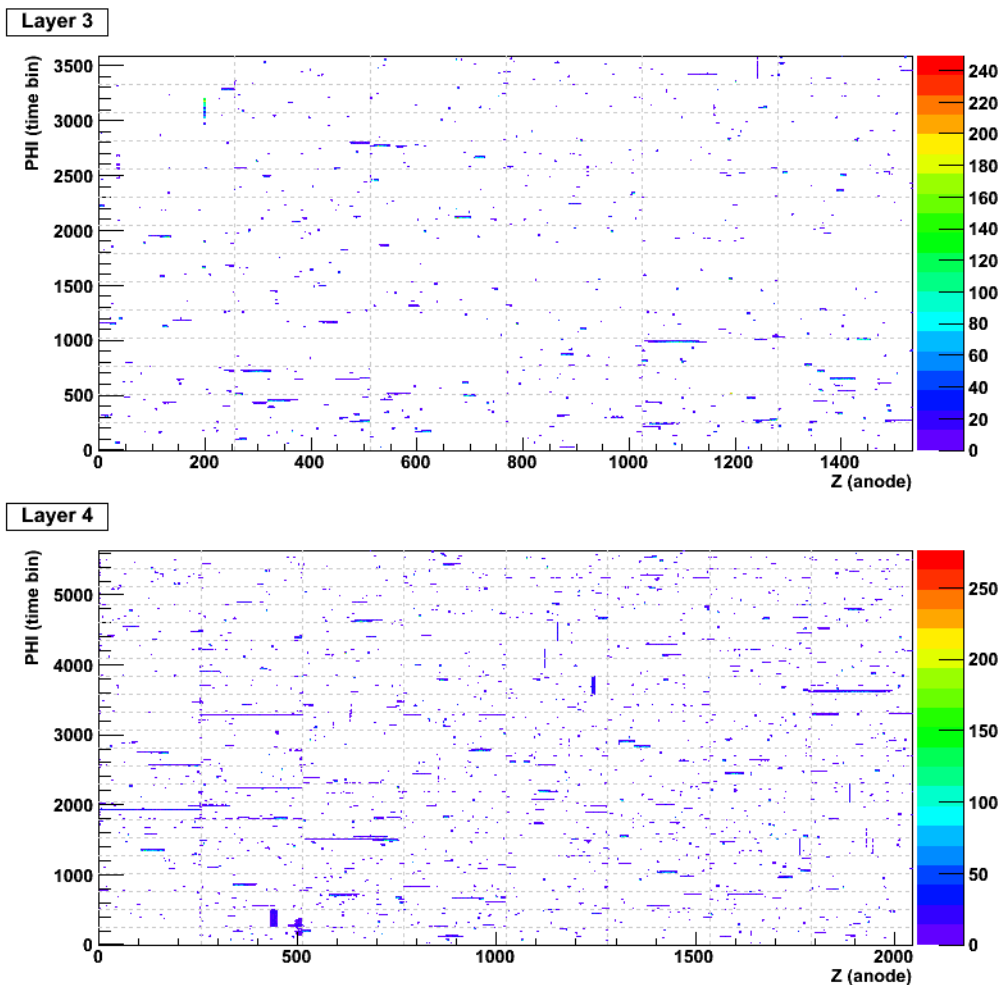
Figure 12. Display of an event collected by the SDD during the T12 injection test. The Z coordinate (along the beam direction) is on the horizontal axis expressed as anode number, while the vertical axis is the φ coordinate, expressed as time bin (25 ns each); the color chart represents the quantity of charge collected by a single anode. Each blue point is a particle hit; continuous lines correspond to particles crossing a whole module along the Z axis.

case would be a sharp rise, is fitted with an error function. The time zero is then extracted from the fit. This procedure provides a direct determination of the time zero and does not require any other calibration parameter such as the drift speed; moreover it is an SDD standalone measurement without any use of information from the other ITS subdetectors. But it has the disadvantage of requiring a large number of reconstructed points.

The second method consists in measuring track-to-point residuals. Muon tracks are fitted in SPD and SSD, using at least 5 points, and the residuals between the track crossing point taken as reference and the cluster coordinate in SDD are computed. The time offset is extracted by exploiting the opposite sign of the residuals in the two detector sides (see figure 1): an uncalibrated time offset would lead to an over/underestimation of the drift path, and therefore to residuals of opposite signs in the two sides. The distance between the two peaks of the distribution of residuals
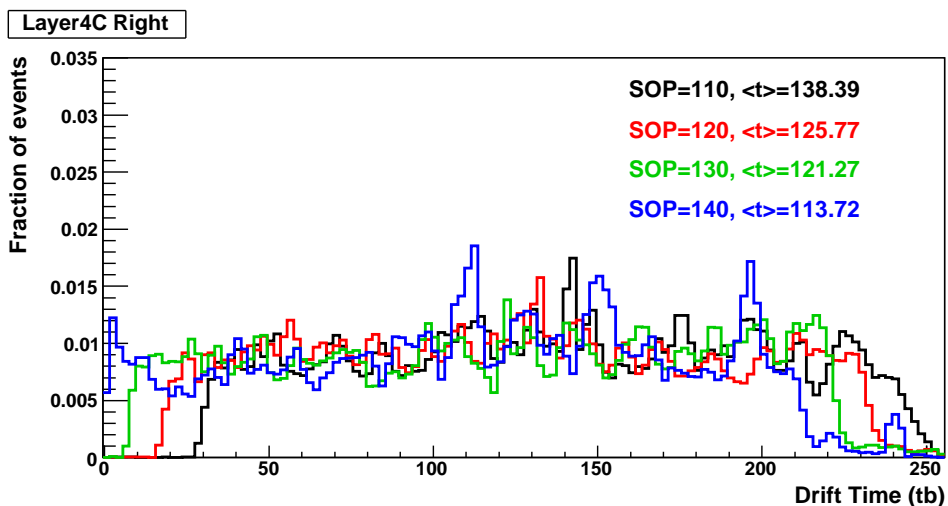
Figure 13. Distribution of the particle drift times on Layer 4 (one half-ladder) sampled at 40 MHz for the four different SOP delay values scanned (peaks are due to particles crossing modules side by side, as seen in figure 12).

in the two detector sides corresponds to $2v_{drift}t_0$, thus leading to the determination of the time zero [19, 20]. This procedure requires less statistics, but relies on calibration parameters (the drift speed and the correction maps, see section 2); moreover, being based on track reconstruction in ITS, it might be biased by SPD and/or SSD misalignments.

As a first approximation the time zero can be considered equal for all modules apart from corrections for different cable lengths: actually a significant difference (~ 25 ns) between the modules in the half ladders located on positive and negative z has been found due to the different optical fiber length (about 6 m).

The time zero calibration is discussed in detail in ref. [19] together with the results of the internal ITS alignment with atmospheric muons.

4.3 Charge calibration

The data sample of cosmic muons collected during the 2008 cosmic run allowed to extract for a subsample of modules the conversion factor from ADC counts to the energy deposited in keV and the dependence of the collected charge on drift time. In figure 14 the module-ladder density map of reconstructed cosmic muons for SDD Layer 3 and Layer 4 is shown; clearly the horizontal modules (around ladder 4 and 11 for Layer 3 and ladder 6 and 17 for Layer 4) have many more entries that the vertical or quasi-vertical ones.

In a silicon drift detector the cluster shape and possibly cluster charge depend on the distance traveled by the electrons from the production point to the collection anodes. Due to the diffusion effect, the gaussian width of the electron cloud grows with the square root of the drift time, thus giving rise, along both anode and drift axes, to a drift time dependent cluster size. For a particle crossing close to the anodes a typical cluster size is 1 anode times 3 time bins (at 40 MHz sampling rate), which increases to 3 anodes times 7 time bins for particles with maximum drift distance.
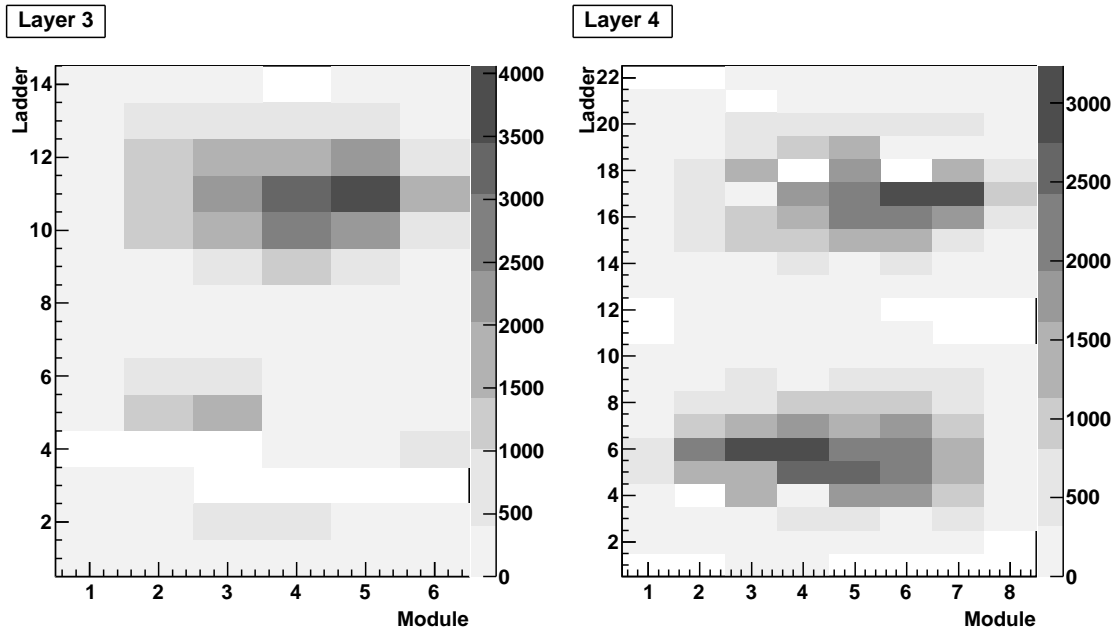
Figure 14. Detector occupancy with reconstructed cosmic muons for Layer 3 (left) and Layer 4 (right). Layer 3 shows less statistics because it was off for about one month due to hardware problems in a read-out electronic crate.
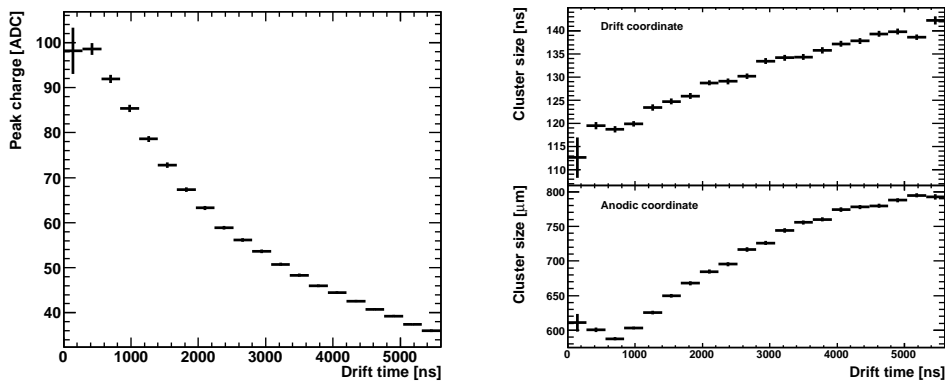

Figure 15. Left: Distribution of charge peak inside a cluster as a function of drift time. Right: cluster size along the two coordinates as a function of drift time.

At the same time, the charge peak in the cluster, i.e. the anode/time bin cell in the cluster with maximum ADC count value, decreases with increasing drift time. This charge diffusion effect is shown in figure 15. The signal-to-noise ratio in the peak is about 50 for clusters close to the anodes and decreases to 20 at the maximum drift lengths.

Due to the zero suppression applied to the counts in the time bin cells, this diffusion effect can also give rise to a dependence of the reconstructed cluster charge on the drift distance. The longer the drift time, the larger the charge diffusion and consequently the larger the fraction of charge in
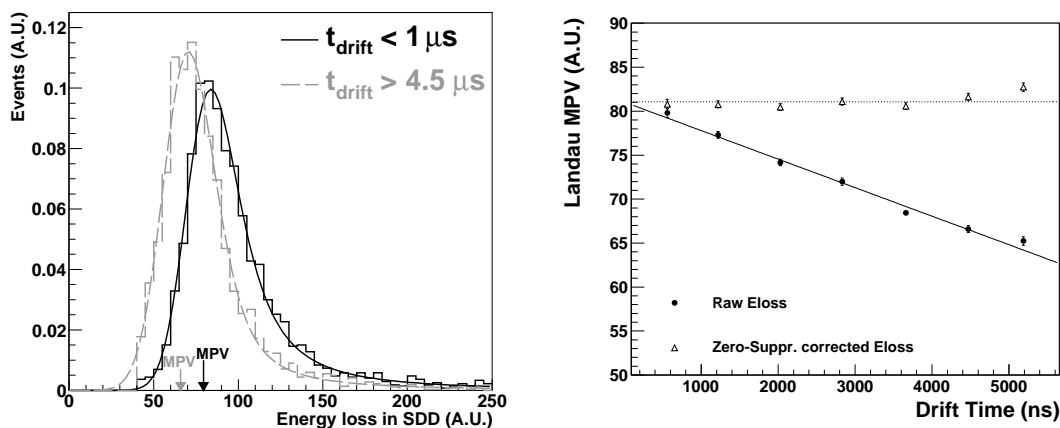
Figure 16. Left: Distribution of energy deposit (in arbitrary units) for clusters reconstructed in the SDD detector for two intervals of drift time. Fits with a convolution of a Landau and a Gaussian are superimposed. Right: Landau Most Probable Value vs. drift time, with and without correction for zero-suppression effect.

the electron-cloud tails which is more easily cut by the zero-suppression algorithm. This effect is shown in the left panel of figure 16 where the energy deposit of SDD clusters in two intervals of measured drift time is reported for a sample of atmospheric muons collected without magnetic field during the 2008 data taking. The shape of the energy deposit distribution is well reproduced by a Landau function convoluted with a Gaussian; the peak of the distribution is located at a lower value of energy for particles with large drift times. In figure 16 right, the Most Probable Value (MPV) of energy deposit extracted from Landau+Gaussian fits in 7 bins of drift time is plotted as a function of drift time (closed circles). A linear correction for this effect has been extracted from detailed simulations of the detector response taking into account the combined effect of electron diffusion and zero-suppression thresholds. By applying this correction to the muon clusters, the Landau MPV results to be independent from drift time, as it can be seen in the right panel of figure 16 (open triangles). Since the trapping effects (causing an actual charge loss in the silicon volume during the drift) are not included in the Monte Carlo simulations used to extract the applied correction, we can conclude that the observed charge dependence on drift time is mainly due to the effect of the thresholds applied by the zero-suppression algorithm. This confirms the results obtained in a laboratory setup on a few spare modules [20, 21].

After correcting for the track inclination, it is possible to extract the ADC-to-keV conversion factor by rescaling the observed MPV to the expected most probable value of energy deposition for a Minimum Ionizing Particle (MIP) crossing 300 μm of silicon. As seen in figure 14, this calibration could be done only for a few modules close to the vertical direction with the cosmic data sample. The obtained conversion factor is compatible (within $15 \div 20\%$) with the value extracted from a detailed MonteCarlo simulation. A full module-by-module calibration will be done with the first p-p data sample.

5 Conclusions

During the 2008 commissioning run with cosmic muons the Silicon Drift Detectors of the ALICE experiment were regularly calibrated in order to determine the baselines, the noise, the gain and the drift speed. All monitored parameters proved to be stable during the entire period (within 1% for the drift speed). Supplementary calibrations for the SOP delay and the time offset were also performed by exploiting the injection test and the reconstructed muon tracks. The detector was fully operational and ready for the planned p-p data taking.

After the major experiment shutdown during the winter, the detector was brought up for the new 2009 commissioning run. Similar calibrations are being performed to monitor the detector performance and measure its working parameters.

References

[1] ALICE collaboration, P. Cortese et al., *ALICE: physics performance report, volume I*, *J. Phys.* **G 30** (2004) 1517.

[2] ALICE collaboration, K. Aamodt et al., *The ALICE experiment at the CERN LHC*, 2008 *JINST* **3** S08002.

[3] P. Giubellino, *Heavy Ion Physics at the LHC*, arXiv:0809.1062.

[4] ALICE collaboration, G. Dellacasa et al., *ALICE Inner Tracking System (ITS): Technical Design Report*, CERN-LHC-99-012.

[5] ALICE collaboration, A. Rashevsky et al., *Characteristics of the ALICE silicon drift detector*, *Nucl. Instrum. Meth.* **A 461** (2001) 133.

[6] S. Beolè et al., *Study of the uniformity of high resistivity neutron doped silicon wafers for silicon drift detectors*, *Nucl. Instrum. Meth.* **A 473** (2001) 319.

[7] A. Rashevsky et al., *Charge injectors of ALICE Silicon Drift Detector*,
Nucl. Instrum. Meth. **A 572** (2007) 125.

[8] D. Nouais et al., *Drift velocity monitoring of SDDs using MOS charge injectors*,
Nucl. Instrum. Meth. **A 450** (2000) 338.

[9] E. Crescio, D. Nouais, P. Cerello, *A detailed study of charge diffusion and its effect on spatial resolution in Silicon Drift Detectors*, ALICE Internal Note ALICE-INT-2001-09.

[10] S. Coli et al., *The cooling system of the Silicon Drift Layers of the ALICE Inner Tracking System*, ALICE Internal Note ALICE-INT-2008-008.

[11] G. Batigne et al., *Characterization of the ALICE Silicon Drift Detectors using an infrared laser*,
2008 *JINST* **3** P06004.

[12] ALICE collaboration, C. Piemonte, V. Bonvicini, A. Rashevsky, A. Vacchi and R. Wheadon, *Electric performance of the ALICE silicon drift detector irradiated with 1-GeV electrons*,
Nucl. Instrum. Meth. **A 485** (2002) 133.

[13] ALICE collaboration, S. Kushpil et al., *Beam test results of the irradiated Silicon Drift Detector for ALICE*, *Nucl. Instrum. Meth.* **A 566** (2006) 94.

[14] D. Cavagnino et al., *Zero Suppression and Data Compression for SDD Output in the ALICE Experiment*, ALICE Internal Note ALICE-INT-1999-28.

[15] S. Antinori et al., *Design and Test of the ALICE SDD Data Concentrator Card CARLOSrx*, in proceedings of *2006 IEEE Nuclear Science Symposium and Medical Imaging Conference*, 29 October – 4 November 2006, San Diego, CA U.S.A.

[16] F. Carena et al., *The ALICE Data-Acquisition Read-out Receiver Card*, in proceedings of *10th Workshop on Electronics for LHC Experiments and Future Experiments*, 13–17 September 2004, Boston, MA U.S.A.

[17] ALICE collaboration, F. Roukoutakis and B. von Haller, *Commissioning of the ALICE-LHC online data quality monitoring framework*, *Nucl. Instrum. Meth.* **A 603** (2009) 446.

[18] A. Colla and J.F. Grosse-Oetringhaus, *The Shuttle Framework – A system for automatic readout and processing of conditions data*, ALICE Internal Note ALICE-INT-2008-011.

[19] ALICE collaboration, K. Aamodt et al., *Alignment of the ALICE Inner Tracking System with cosmic-ray tracks*, 2010 *JINST* **5** P03003;
see also C. Bombonati et al., *Alignment of the ALICE Inner Tracking System with cosmic-ray tracks* , ALICE Internal Note ALICE-INT-2009-035.

[20] F. Prino for the ALICE collaboration, *Operation of the Silicon Drift Detector of the ALICE Inner Tracking System during cosmic runs*, in proceedings of *RD09 – 9th International Conference on Large Scale Applications and Radiation Hardness in Semiconductor Detectors*, 30 September – 2 October, 2009, Florence, Italy [PoS(RD09)007].

[21] B. Alessandro et al., *Charge collection in the Silicon Drift Detectors of the ALICE experiment*,
2010 *JINST* **5** P02008.